ROYAL SOCIETY
OF CHEMISTRY

PAPER

Check for updates

Carbonised porous silicon as scaffold and sensor for the electrochemical detection and characterisation of bacterial biofilm growth

Fearghal O'Connor,[ab] Alexandros Lazanas [ID] *[a] and Beatriz Prieto Simón [ID] *[ac]

The use of carbonised porous silicon (C-pSi) substrates as both scaffolds and electrodes for the electrochemical detection and characterisation of bacterial biofilm growth is reported for the first time. Three types of C-pSi are presented showcasing versatility in their hydrophilicity and surface chemistry. The tunability of these properties is taken as a springboard for the biological, morphological and electrochemical evaluation of the biofilms. The combined characterisation data obtained from environmental scanning electron microscopy, confocal scanning laser microscopy, cyclic voltammetry and electrochemical impedance spectroscopy, confirm C-pSi as a powerful tool for sensing bacterial biofilm growth. The collective assessment of biofilm growth at the C-pSi surface reveals changes related both to morphological and temporal parameters.

1. Introduction

Bacteria are ubiquitous single-cell microorganisms that exhibit a wealth of characteristics facilitating their survival in a wide range of environments. While there are many ways in which bacteria can be classified, they basically exist in one of two interchangeable states: (1) planktonic or free floating and (2) sessile or immobile. The sessile state is by far the most common state in which bacteria are found whereby they are bound to a surface or to each other, and encased in a self-produced extracellular matrix (ECM) of proteins, lipids and extracellular DNA fragments.[1–4] The combination of bacteria or microbial community and this ECM is known as a biofilm.

The formation of biofilms is a complex and finely regulated process. Laboratory models explain the formation process as happening in five sequential steps: (1) initial reversible attachment, (2) irreversible attachment and surface colonisation, (3) microcolony development, (4) biofilm maturation, and (5) dispersal. While this five-step model functions as a good general depiction of how biofilms grow *in vitro*, it fails to capture the complexity of biofilms that are found in natural, clinical and industrial settings. A recent review by Sauer *et al.*[5] expands on this model, capturing more of the nuances observed in biofilm microbiology.[5]

Many advantages are imparted to the organisms residing in biofilms, mainly increased survivability, microenvironment creation and encouraging symbiotic relationships. The biofilm matrix not only provides a physical barrier to an (often harsh) external environment but also a diffusion barrier for antimicrobial compounds.[6,7] The microenvironment within biofilms facilitates horizontal gene transfer whereby genetic information can be transferred between microorganisms embedded in the ECM without the need for the production of new offspring.[8] This allows for the fast spreading of antimicrobial resistant genes.[9] A review by Flemming *et al.*[10] describes the emergent properties of biofilms and how they contribute to the above-mentioned characteristics.[11]

A wide range of both industrial and clinical fields are negatively impacted by the formation and recalcitrance of biofilms. A major economic burden can be attributed to biofilms with an estimated annual cost of $5 trillion globally.[12] Shipping, energy and water distribution are the industries that are most affected by biofilms, as they can passivate surfaces (*i.e.*, cause surface biofouling), contaminate water sources, and are implicated in the corrosion of metallic equipment and pipes.[13,14]

Behind the economic burden is an alarming and growing impact on the health sector. Persistent biofilms are present in chronic wounds, preventing natural healing processes.[15] They can form on medical devices leading to infection, device failure and the need for device replacement.[16] Of great concern is the high resistance of biofilms to antimicrobial agents (up to 1000 times higher than that of planktonic cells) and their role in favouring the emergence and spread of antimicrobial

[a] *Institute of Chemical Research of Catalonia, The Barcelona Institute of Science and Technology, Av. Països Catalans 16, 43007, Tarragona, Spain.*
  E-mail: alazanas@iciq.es, bprieto@iciq.es
[b] *Universitat Rovira i Virgili, 43007, Tarragona, Spain*
[c] *ICREA, Pg. Lluís Companys 23, 08010, Barcelona, Spain*

resistance by promoting horizontal transfer of resistance genes.[7,17] As biofilms mature, they become difficult to eradicate by physical or chemical means, making early detection vital for the implementation of successful eradication strategies.

Current biofilm detection methods are based on culturing technologies, molecular assays and microscopy.[18] While these methods provide sound results and have advanced our understanding of the nature of biofilms, they do have some significant limitations. Invasiveness, cost and turnaround time for results are their main drawbacks.[19] This highlights the need for novel and highly efficient biofilm detection methods. Biosensors offer potential for use in this field as they can be designed to be cost-effective, non-invasive, rapid and allow for real-time monitoring.[20,21]

Electrochemical biosensors further press the advantages offered by biosensors over conventional detection and characterisation methods. Their detection capabilities can be expanded beyond end-point analysis allowing for full characterisation of the biofilm formation process to be realised. Heightened specificity and selectivity make the possibility of early detection a reality, which has proven challenging using the current methodologies. Here we describe the in-house fabrication of a carbonised mesoporous silicon (C-pSi) substrate with a dual function: (i) as a scaffold to grow bacterial biofilms, and (ii) as a working electrode to electrochemically monitor the aforementioned growth. Three types of C-pSi were fabricated. Two types were carbonised using acetylene gas as a carbon source: a hydrophobic variant, termed thermally hydrocarbonised pSi (THC-pSi), and a hydrophilic variant, termed thermally carbonised (TC-pSi).[23] The third C-pSi variant, termed polymer carbonised pSi (PC-pSi) is produced through the deposition of furfuryl alcohol onto the pSi surface, followed by its polymerisation and pyrolysis (the term PC-pSi is used here to maintain consistency between different C-pSi substrates; this variant has been referred to as poly(furfuryl alcohol) pSi or PFA-pSi in a previous study from our group[24]). PC-pSi has been shown to possess mildly hydrophilic surface characteristics, which serves as a middle ground between TC-pSi and THC-pSi. The difference in surface wettability of each C-pSi is investigated here as a growth factor over different timescales. This is monitored *via* contact angle measurements before and after 24 h, 48 h and 72 h of bacterial biofilm growth. The same timescale is used for every biofilm growth characterisation method employed in this work. To assess the suitability of each substrate as a biofilm growth scaffold, environmental scanning electron microscopy (ESEM) and confocal laser scanning microscopy (CLSM) are carried out. Importantly, the value of the three types of C-pSi substrates as electrochemical signalling platforms was already proven in published studies,[23,24] facilitating their use as electrodes to monitor biofilm growth. This is accomplished by employing cyclic voltammetry (CV) and electrochemical impedance spectroscopy (EIS). In both cases, hexammineruthenium(III) chloride (Ruhex) was chosen as redox probe. This choice was due to the outer-sphere characteristics of Ruhex which negates the effect of surface chemistry on its electrochemical behaviour (in contrast with the regularly employed hexacyanoferrate(II/III)).[25] In this context, CV is used to correlate the difference in surface coverage in the different stages of biofilm growth with the deviation of voltammetric peak current. Additionally, CVs at different scan rate values are recorded to provide insight into the diffusion regime in each system which can be dependent to the morphological characteristics of the biofilm. Correspondingly, EIS is used to study the impedance of the electrochemical system over a broad frequency range. Given the procedural generation of biofilm over time on the electrode surface, EIS is a valuable tool used here to quantify changes in the electrode environment with respect to charge transfer, double-layer capacitance and diffusion processes.

To demonstrate the potential of C-pSi for the electrochemical detection of biofilms, *Staphylococcus epidermidis* (*S. epidermidis*) is selected for this work due to the ease of biofilm growth in laboratory models. *S. epidermidis* is a Gram-positive coccus species of bacteria that is typically found as part of the human skin microbiota and on various mucosal membranes. When found in these environments *S. epidermidis* has a beneficial role for humans mainly by outcompeting potential pathogens and modulating the host immune response.[22] However, even commensal strains have been shown to be resistant to antibiotic agents and, coupled with a strong biofilm forming ability, they can become opportunistic pathogens themselves.[22]

The end goal of this work is the complete characterisation of *S. epidermidis* biofilm growth processes on C-pSi scaffolds which are able to act simultaneously as electrochemical transducers. The conjunction of bioassays with advanced microscopy and electrochemical techniques is expected to contribute significantly to pinpointing of the appropriate conditions for biofilm growth monitoring and sensing, leading to advanced bioactive platforms.

2. Experimental

2.1. Materials

S. epidermidis ATCC 1798 was used for all culturing related experiments. p-type Si wafers with 0.00055–0.001 Ω cm resistivity, (100)-oriented were purchased from Siltronix (France). Hydrofluoric acid (48%, ACS Grade) was a product of Supelco. Sodium hydroxide pellets were purchased from Merck. Absolute ethanol was purchased from Scharlau. The acetylene gas cylinder (2.6 atomic adsorption grade) was purchased from Linde. Furfuryl alcohol (98%), oxalic acid (98%), hexammineruthenium(III) chloride (Ruhex), phosphate buffer saline (PBS) tablets, tryptic soy broth (TSB), and tryptic soy agar were products from Sigma-Aldrich. LIVE/DEAD™ BacLight™ Bacterial viability kit was a product from Thermo Fischer Scientific. Ethanol (96% v/v) was purchased from PanReac AppliChem. MilliQ water was used throughout.

2.2. pSi fabrication

Three types of C-pSi substrates were fabricated for this work: (i) thermally hydrocarbonised pSi (THC-pSi), (ii) thermally carbonised pSi (TC-pSi), and (iii) polymer carbonised pSi (PC-pSi). The initial etching procedure for each substrate remained the same. Electrochemical etching of the Si substrates was carried

out by a two-step anodisation process. The cell set-up included a platinum electrode (cathode) and the p-type Si wafer (anode). The etching solution was made up of HF as the etchant and absolute ethanol as a surfactant to reduce the surface tension between the Si wafer and the solution, allowing the HF to interface with the Si. The first anodising step electropolished the surface of the Si wafers with a current density of 220 mA cm^{-2} (corresponding to 353 mA) for 30 s in a 3:1 (v/v) aqueous HF (48%):EtOH solution generating a sacrificial layer. Next, the anodisation solution was removed, and the cell was thoroughly washed with EtOH and dried under nitrogen flow. The sacrificial layer was removed by immersing the anodised Si in 5 M NaOH for 5 min. Then, NaOH was removed and the same cleaning process as above was followed. The second anodisation was conducted by applying a current density of 47 mA cm^{-2} (76 mA) for 150 s, using a 1:1 (v/v) aqueous HF (48%):EtOH solution. Finally, the cleaning protocol was followed again and the sample was ready for the carbonisation process.

2.3. pSi carbonisation

THC-pSi was produced following the thermal process described by Salonen *et al.*[26] with some modifications. The freshly etched pSi substrates were cut into 1.5 cm × 1.5 cm pieces and placed into a quartz tube under nitrogen flow at 2 L min^{-1} for 45 min at room temperature. A 1:1 nitrogen/acetylene mixture flow was introduced into the tube at room temperature for 15 min after the purging step, then the quartz tube was placed into a preheated tube furnace at 525 °C for 17 min under the continuous mixture flow. After the THC process, the tube was left to cool down under nitrogen flow.

TC-pSi carbonisation was conducted in a similar manner with the addition of an annealing step to the THC-pSi process, consisting of applying 800 °C for 9 min only under nitrogen flow (2 L min^{-1}). Finally, the tube was left to cool back to room temperature under nitrogen flow.

Finally, for PC-pSi, freshly etched pSi samples were spin-coated with a 1:1 (v/v) furfuryl alcohol (FA):EtOH solution, containing 5 mg mL^{-1} oxalic acid used as polymerisation catalyst. Spin coating was done in two steps, first at 400 rpm for 2 min to infiltrate FA into the porous structure, and then at 4000 rpm for 1 min. Subsequently, FA-coated pSi samples were placed into a quartz tube under nitrogen flow at 2 L min^{-1} for 15 min at room temperature. Then, the temperature was increased with a ramp rate of 5 °C min^{-1} up to 100 °C which was maintained for 2 h to thermally polymerise FA. Next, the temperature was further increased with a ramp rate of 15 °C min^{-1} up to 700 °C to pyrolyse the polymer. At this stage, the temperature was kept constant for 2 h and 20 min. Finally, the tube was cooled back to room temperature under nitrogen flow.

2.4. pSi characterisation

Imaging of C-pSi was carried out by a Scios 2 (FEI) field emission scanning electron microscope (FESEM) using an accelerating voltage of 5 kV. An Ossila Contact Angle Goniometer (Leiden, The Netherlands) was used for water contact angle measurements. A 25 μL syringe was used to dispose sterile MilliQ water droplets onto the surface of the pSi substrates. Measurements were taken in triplicate at three positions for each sample.

2.5. Biofilm growth on C-pSi

S. epidermidis biofilms were grown on the C-pSi substrates by using the double culture technique. 1 mL of the stock solution (details in the SI) was added to a falcon tube with 9 mL of freshly autoclaved (and cooled to room temperature) TSB media. This was then placed in an incubator overnight (15 h) at 37 °C. This step increased the population of bacteria in the solution (to 1 × 10^5 CFU mL^{-1}) and limited the incubation to 15 h ensuring that the bacteria were still in their log phase of growth. The solution was then centrifuged at 4000 rpm for 10 min and the supernatant was discarded. The pellet was then resuspended in 10 mL of fresh TSB media. 200 μL of this solution was pipetted onto the C-pSi surface to seed the biofilm growth. Samples were then covered and incubated at 37 °C. Sterile media was pipetted onto the surface of the substrates as controls instead of the media/bacteria solution.

2.6. Biofilm characterisation *via* environmental scanning electron microscopy

After incubation, samples were washed with sterile MilliQ water to remove remaining media and any unattached cells, then left to dry for 15 min at room temperature. Samples were fixed incubating 5% glutaraldehyde prepared in 0.1 M sodium cacodylate buffer (pH 7.5) for 24 h at 4 ± 2 °C. The fixative was decanted, and the samples were rinsed with sterile MilliQ water again. The samples were loosely covered and were left to dry for 72 h under a fume hood at room temperature. Before imaging, the samples were sputter coated with approximately 10 nm of gold *via* a Quorum Q150T S Plus sputter-coater system. Imaging was carried out by a Quanta 600 (FEI) scanning electron microscope using an accelerating voltage of 20 kV, and a vacuum pressure of 5.67 × 10^{-4} Pa.

2.7. Confocal imaging and viability testing

When the desired incubation time was reached the samples were gently rinsed with sterile MilliQ water to remove any unattached or loosely attached bacteria and left to dry for 15 min at room temperature. To preserve the 3D structure of the biofilms, the samples were bathed in a fixative 2% glutaraldehyde solution, prepared in 0.1 M PBS, pH 7.4. After 30 min incubation, the fixative solution was removed, and the samples were rinsed again with sterile MilliQ water. The samples were stored at 4 ± 2 °C before staining and imaging. Staining was carried out immediately prior to imaging to prevent the dyes from losing their fluorescence bleaching. SYTO® 9 and propidium iodide stains were prepared as per the LIVE/DEAD™ BacLight™ Bacterial viability kit instructions. 3 μL of each stain was added to 1 mL of sterile MilliQ water. 150 μL of this staining solution was applied to each test sample and incubated at room temperate for 30 min protected from light.

Samples were imaged with CLSM (LSM 980 Airyscan 2, Carl Zeiss Microscopy, Germany) using a 63× oil immersion objective. The excitation/emission was 495 nm/<613 nm for SYTO® 9 and 257 nm/>525 nm for propidium iodide. Two channels were used for separate imaging of the green and red stains. The imaging

11286 | *J. Mater. Chem. B*, 2025, **13**, 11284–11297

This journal is © The Royal Society of Chemistry 2025

started at the top surface of the biofilm and finished at the biofilm-C-pSi interface.

The images were analysed by using the Fiji software (ImageJ, US National Institutes of Health, Bethesda, Maryland, USA) and Zeiss ZENlite 3.11 (Jena, Germany).

2.8. Electrochemical measurements

Electrochemical measurements were conducted with an Ivium-n-STAT electrochemical analyser (Ivium technologies BV) with a conventional 3-electrode cell. C-pSi electrodes, both samples and controls, were used as the working electrode, while an Ag/AgCl 3 M KCl electrode and a platinum wire served as the reference and the counter electrode, respectively. CVs were recorded in 0.1 M PBS, pH 7.4, at a scan rate of 0.1 V s^{-1} (unless otherwise stated). EIS spectra were recorded in 0.1 M PBS over the frequency range from 10 kHz to 0.1 Hz using a sinusoidal excitation signal of 10 mV (rms). The applied DC potential was -0.2 V and the redox couple (hexammineruthenium chloride – Ruhex, $C = 10$ mM) was used throughout the electrochemical measurements.

3. Results & discussion

3.1. Characterisation of C-pSi electrodes

Morphological characterisation was conducted *via* FESEM to determine pore size and depth of each C-pSi platform (Fig. S1). Starting with TC-pSi, the average pore size was *ca.* 34 ± 7 nm with the average pore length being *ca.* 3.5 μm. The respective PC-pSi sample had an average pore size of *ca.* 21 ± 5 nm with an average pore length of *ca.* 3.5 μm. Finally, THC-pSi had an average pore size of 42 ± 13 nm, with the average pore length being also *ca.* 3.5 μm (note that pore length is dependent on the duration of the second anodisation step and is expected to be the same for all platforms, while the pore size can variate depending on each carbon coating).

The desideratum behind using the three types of C-pSi substrates, to demonstrate their potential to act both as bacterial biofilm scaffold and electrochemical transducer to sense biofilm growth, lies in their varied surface chemistry which is reflected in the differences in wettability they show. Contact angle measurements were employed to illustrate the difference in wettability for each C-pSi which was expected to impact significantly on biofilm growth. TC-pSi, PC-pSi, and THC-pSi cover a broad range of wettabilities (Fig. S2 depicts their respective contact angles). The contact angle of $30.4 \pm 1.3°$ for TC-pSi proves its hydrophilic nature, while PC-pSi exhibiting a contact angle of $50.7 \pm 3.7°$ lies in the middle between TC-pSi and hydrophobic THC-pSi ($95.9 \pm 3.3°$). To conclude, we have ascertained that the three platforms deviate incrementally between hydrophobic and hydrophilic behaviour, in a fashion that can be used to successfully discriminate between different biofilm growth patterns on C-pSi surfaces.

3.2. Microscopy analysis of biofilm growth

Environmental scanning electron microscopy (ESEM) is the preferred choice of electron microscopy to analyse biofilms as it is not required to be operated under a high vacuum nor does the surface to be analysed need to be conductive.[19] Fixation techniques are used to retain the natural integrity of the biofilm under analysis. Similar to conventional SEM, ESEM can provide detailed images at high magnifications for qualitative evaluation of biofilm presence, formation kinetics and spatial characteristics.[19] ESEM is limited to generating images from the surface of the 3D biofilms and any information or data obtained generally support separate quantitative analysis carried out. In contrast with ESEM, confocal laser scanning microscopy (CLSM) provides in-depth analysis of the biofilm and uses z-stacks to generate 3D images. CLSM can be easily combined with viability staining to differentiate alive and dead bacterial cells. Significantly, this facilitates the assessment of the impact of the substrate on cell proliferation. The combined use of ESEM and CLSM provides all the essential information to assess the suitability of each C-pSi substrate as a scaffold for biofilm growth.

The presence of biofilm growth on the three types of C-pSi was confirmed by ESEM imaging (Fig. S3 shows ESEM images upon 24 h, 48 h and 72 h of biofilm growth). Cells were confirmed to attach to all substrates by 24 h. Information on bacterial cell morphology, organisation and biofilm growth pattern was obtained. *S. epidermidis* cells were observed on the topical surface of the biofilm growing in typical coccus fashion and with the absence of other shaped cells or micro-organisms. These observations confirm that our culturing protocols were successful in growing a mono-species *S. epidermidis* biofilm. In addition, features such as cracks or fissures were also observed along with areas which were out of focus suggesting that the surface topography was heterogenous.

Fig. 1 illustrates the CLSM profiles of the *S. epidermidis* biofilms on the three types of C-pSi over 24 h (left), 48 h (centre), and 72 h (right) of biofilm growth. Growth patterns and architectural features were analysed qualitatively, while surface coverage (confluence), cell density and biofilm thickness were quantified *via* analysis of CLSM images as explained in Section 2.7. The respective CLSM images of the control groups without any biofilm on the surface are shown in Fig. S4.

From a morphological perspective, the biofilm on TC-pSi exhibits mushroom or hill-like structures at 24 h, while by 48 h and 72 h the 3D structure becomes progressively more homogeneous, although still retaining a small degree of heterogenicity. Patchy growth patterns are observed for the biofilm on PC-pSi grown for 24 h, whereas at 48 h and 72 h the growth pattern becomes more confluent while retaining a heterogenous surface topography. Also, a pore is observed in the 72 h sample (Fig. 1F). A more homogeneous growth pattern was observed for the biofilm on THC-pSi for all time points. However, cavities were observed in both the 24 h and 48 h samples with full gaps being observed for the 72 h sample.

Confluence was measured by using ImageJ software to analyse CLSM images. The biofilm on TC-pSi had the lowest confluence % after 24 h of growth (59.3%), before reaching almost complete surface coverage at 72 h (>99%). The biofilm on PC-pSi reached 86.7% at 24 h growth, before peaking at 98.1% at 48 h. Finally, the biofilm on THC-pSi achieved almost complete surface coverage after 24 h, with >99% at 72 h.
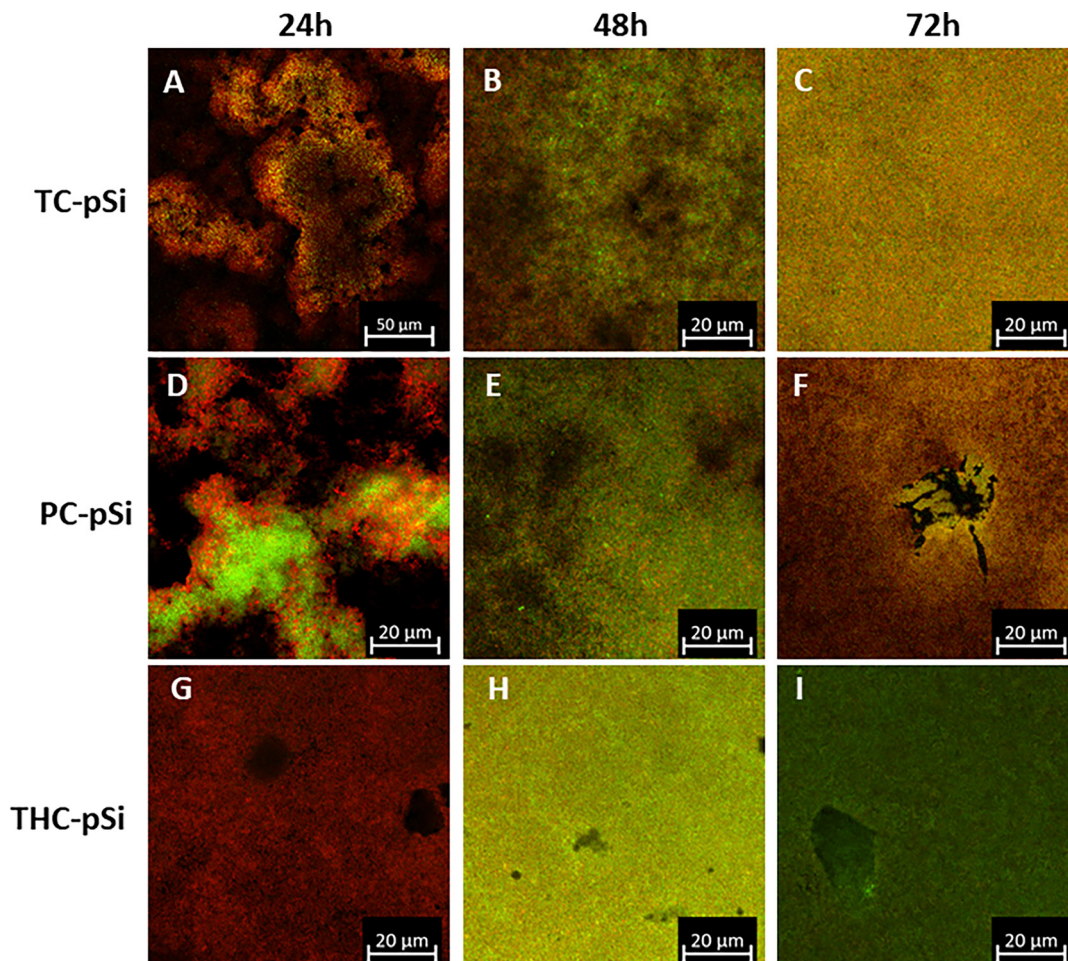
This journal is © The Royal Society of Chemistry 2025

J. Mater. Chem. B, 2025, **13**, 11284–11297 | **11287**

Fig. 1 CLSM images of the biofilms grown on TC-pSi, PC-pSi, and THC-pSi after 24 h (left), 48 h (centre), and 72 h (right) of growth.

Cell viability was determined by quantifying the green and red fluorescence intensity (FI) of SYTO® 9 and propidium iodide, signifying alive and dead bacteria cells, respectively. FI measurements combined with confocal z-stacks not only show the average cell viability in the biofilm grown on each C-pSi, but also the spatial distribution of both alive and dead cells within the biofilm. Fig. 2 depicts the mean values of the FI along the z axis of biofilms grown on C-pSi (three electrodes of each type) stained with propidium iodide accounting for dead bacteria cells and SYTO® 9 dye accounting for alive bacteria cells. The FI measured for the biofilms grown on all C-pSi substrates shows the highest values in the centre of the biofilms. A progressive increase in both red and green FI from 24 h to 48 h, and then 72 h is observed for biofilms grown on TC-pSi. A similar trend is observed for THC-pSi. On both substrates, intensity for the green dye is much lower than that
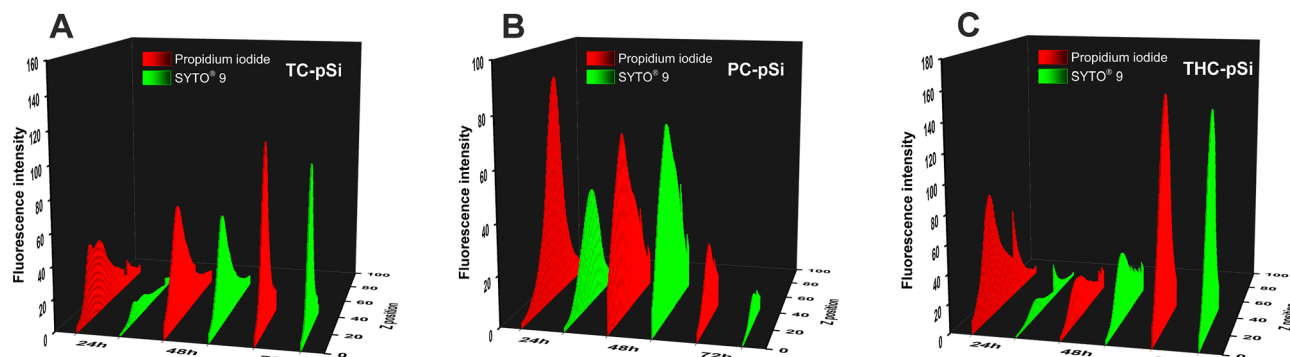

Fig. 2 Plots of FI, from the top biofilm surface to biofilm–C-pSi interface, extracted from the CSML images acquired for biofilms grown during 24 h, 48 h and 72 h onto (A) TC-pSi, (B) PC-pSi, and (C) THC-pSi, using propidium iodide as a dead bacteria stain and SYTO® 9 as the alive bacteria stain.

11288 | *J. Mater. Chem. B*, 2025, **13**, 11284–11297

This journal is © The Royal Society of Chemistry 2025

of the red dye at 24 h, but then by 48 h and 72 h the green intensity is almost equal to that of the red dye. Considering the trend for the green dye independently, this can be explained by the growth rates of bacteria as described above in Section 3.2. The hydrophobic surface of THC-pSi may indirectly account for the high red FI values as the nutrients in the culture media solution are rapidly removed from the surface microenvironment, thus limiting their availability to the bacteria initially attached to the surface. This effect reduces over time as planktonic cells in solution then bind to dead bacterial cells instead directly to the substrate while the biofilm entraps nutrients available for the residing microbes. While for TC and THC-pSi an increasing trend is observed when comparing intensity values at the first time point (24 h) to those at the endpoint (72 h), PC-pSi shows the opposite trend with a significant drop in intensity observed at 72 h. Dead bacteria cells and the related cellular debris offer a new substrate for attachment to the viable planktonic cells that are still in solution.[27] Biofilms that are anchored on dead bacterial cells show changed properties, as reported by Wang *et al.*,[28] who demonstrated a softer, more fluid like biofilm with a lower population of cells when grown on dead bacterial cells as opposed to being anchored to the underlying substrate *via* alive, viable bacterial cells. As there is a relatively high intensity associated with dead bacteria observed after 24 h, we hypothesise that this phenomenon combined with the patchy growth patterns (unique to PC-pSi) explains the intensity drop observed at 72 h due to easier removal (sloughing off) of parts of the biofilm prior to analysis.

The CLSM images depicted in Fig. 1 were also used to estimate the thickness of the biofilms, corresponding to the distance measured between the confocal plane, where the outermost surface of the biofilm becomes visible, and that showcasing the C-pSi surface. Biofilms grown on TC-pSi had their maximum thickness observed after 24 h, before a significant reduction in thickness for 48 h and 72 h measurements (Fig. S5 in the SI illustrates the thickness of biofilms on each C-pSi substrate). The mushroom or hill-like structures observed for biofilms grown on TC-pSi after 24 h may account for the initial high thickness readings, and the subsequent disappearance of those structures and reduction in thickness show that

biofilms change and remodel themselves over time, even under static growth conditions. Less variance in biofilm thickness between the set time points is observed for PC-pSi and THC-pSi. A slight biofilm thickness increase is observed from 24 h to 48 h for both substrates, however, biofilm thickness is reduced at 72 h for PC-pSi whereas the trend on slightly increasing thickness continues for THC-pSi.

3.3. Electrochemical analysis

The key novelty of the work lies in demonstrating the potential of C-pSi to electrochemically analyse the evolution of biofilms grown on its surface. To that purpose, extensive CV and EIS studies were performed. In each case, three C-pSi electrodes of each type were used, and the analysis was performed using the mean values of each electrochemical parameter assessed with the associated standard deviation.

Fig. 3 shows the voltammetric comparison of the three C-pSi platforms in the presence of a redox active compound (Ruhex), at different stages of biofilm growth (before, after 24 h, 48 h, and 72 h). In all cases, a well-shaped cyclic voltammogram is acquired in the absence of biofilm (black lines). The percentage of surface coverage ($\Theta\%$) for each specific C-pSi substrate was calculated at each specific time point of biofilm growth using the following equation:

$$\Theta\% = \frac{I_{pc(before)} - I_{pc(after)}}{I_{pc(before)}} \times 100 \qquad (1)$$

where $I_{pc(before)}$ is the peak current of the forward peak of the redox reaction (for Ruhex, this is the cathodic peak) before biofilm growth, and $I_{pc(after)}$ refers to the respective peak current at each growth stage (24 h, 48 h, or 72 h). Fig. 4 depicts the calculated $\Theta\%$ values for TC-pSi, PC-pSi, and THC-pSi. Red bars correspond to sensors prepared by growing *S. epidermidis* biofilms on each C-pSi substrate during 24 h, 48 h and 72 h. Black bars belong to the respective controls, prepared by incubating each C-pSi substrate in sterile TSB media. Three sensors and three controls were used for each C-pSi type to calculate the mean $\Theta\%$ value with the standard deviation representing the associated error. All controls show $\Theta\%$ values less than half of the value of the corresponding sensors. Results show that $\Theta\%$ reaches its maximum fairly early at the growth
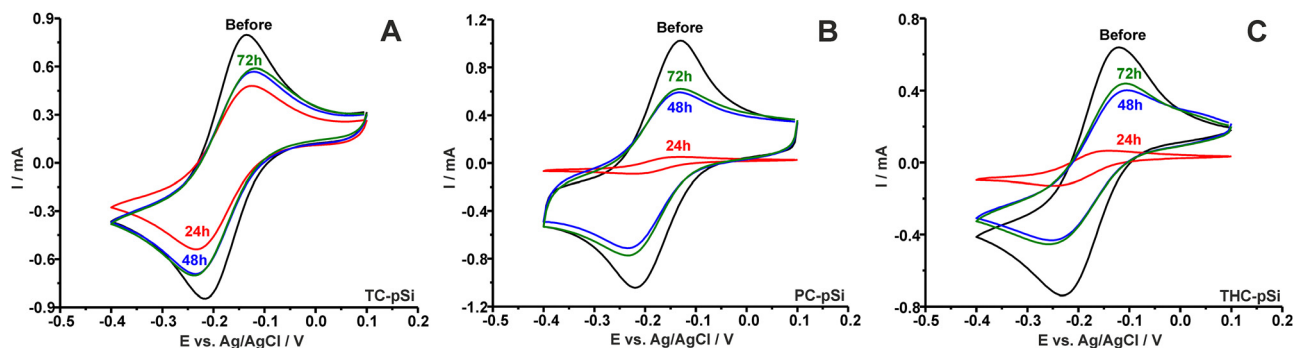

Fig. 3 Cyclic voltammograms obtained using (A) TC–pSi, (B) PC–pSi, and (C) THC–pSi as the working electrode, measured at different stages of biofilm growth, in the presence of 10 mM Ruhex. Electrolyte: 100 mM PBS. Scan rate: 0.1 V s^{-1}.

This journal is © The Royal Society of Chemistry 2025

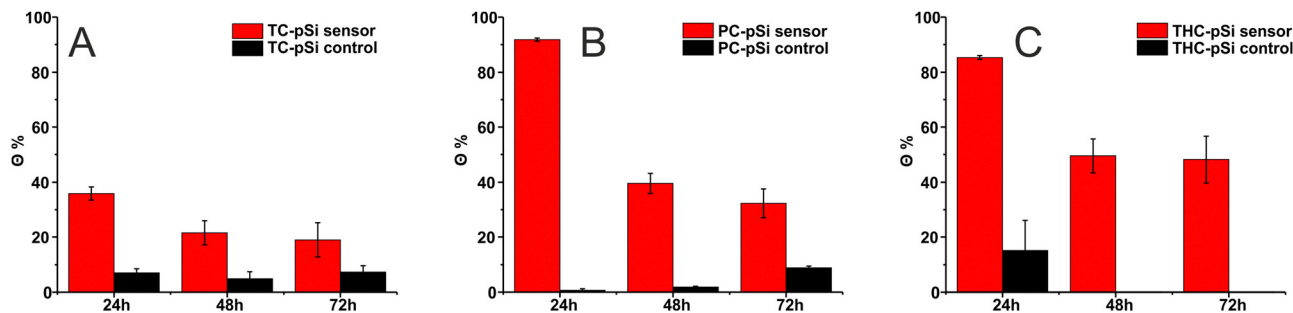*J. Mater. Chem. B*, 2025, **13**, 11284–11297 | **11289**

Fig. 4 Relative surface coverage (Θ%) calculated for (A) TC-pSi, (B) PC-pSi, and (C) THC-pSi with biofilms grown over 24 h, 48 h and 72 h. Red and black bars correspond to sensors and controls, respectively (controls were exposed to the same biofilm growing conditions but in the absence of bacteria). The error bars represent the standard deviation of the measurements for three electrodes.

stage (at 24 h) at all C-pSi electrodes. Among them, PC-pSi and THC-pSi exhibit the highest Θ% ($91.8 \pm 5.7\%$ and $85.2 \pm 6.9\%$, respectively), while the Θ% at the TC-pSi is relatively low ($35.9 \pm 2.4\%$). At 48 h, the Θ% decreases to roughly half of the Θ% measured at 24 h for all the electrodes, (TC-pSi, $21.5 \pm 4.4\%$; PC-pSi, $39.6 \pm 3.6\%$; THC-pSi, $49.5 \pm 6.1\%$), with PC-pSi and THC-pSi exhibiting the greatest coverage among them. These results remain fairly consistent at 72 h (TC-pSi, $18.9 \pm 6.2\%$; PC-pSi, $32.3 \pm 5.2\%$; THC-pSi, $48.2 \pm 8.5\%$).

At first glance, these results may seem to be asymmetrical to the CLSM (Fig. 1) for PC-pSi and THC-pSi (while they follow the same trend for TC-pSi) which have a relatively stable thickness over time. This is because the term "surface coverage" refers to the relative coverage of the electrode surface by a blocking element, inhibiting by extension the charge transfer between the redox species and the electrode. However, according to the voltammetric theory of heterogeneous electrode surfaces,[29,30] there are two factors which influence the voltammetric profile of a partially blocked electrode (such as an electrode surface blocked by a biofilm). The first factor to consider is the percentage of coverage, depending on which the voltammetric peak current is expected to be reduced in magnitude due to charge inhibition by the deposited film. The second factor depends on the morphological features of the blocking film even for the same surface coverage. In general terms, if the blocking film inhibits charge on the surface in a homogeneous fashion (a single macroblock without gaps), then a large decrease in current is expected. In this case, since there are no gaps (the electrode surface is planar), and the diffusion of the electroactive species is linear. However, if the electrode is covered with micrometer-sized blocks (so the uncovered or active part of the electrode is in the same size scale) with micrometer centre-to-centre separations, then the decrease in current is less and the mass-transfer regime may be influenced by radial diffusion effects. Even for this case, radial diffusion is not guaranteed and is subject to the relative mean size of the active part (d_0) to the relative distance between the micrometer-sized blocks (D_0).[29] Radial diffusion will dominate if the diffusion layer thickness (L) is larger than d_0 but smaller than D_0.[29] For a known scan rate (v), L can be calculated by:[30]

$$L = \sqrt{\pi D t} = \sqrt{\pi D \frac{\Delta E}{v}} \qquad (2)$$

where, D is the diffusion coefficient of the electroactive species in cm^2 s^{-1}, $\frac{\Delta E}{v}$ is the width of the voltammetric peak (given in mV) divided by the v (given in mV s^{-1}). The cases where $L < d_0$ or $L > D_0$ the diffusion regime becomes linear again.

Finally, if the electrode is covered by an array of nano- to micrometer-sized blocks, then the impact on the peak current is negligible and the mass-transfer regime is again linear ($L \gg D_0$ for all v).[29] It needs to be stressed that these assumptions only apply to cases with the same percentage of surface coverage. That means that Θ% by definition cannot singlehandedly provide the complete picture of the biofilm morphology and coverage. To complete that picture, here the mass-transfer behaviour of each system was examined by extending the CV studies at increasing v. More specifically, the cyclic voltammetric behaviour of Ruhex was examined over a v range spanning from 5 to 500 V s^{-1} (for the respective CV responses see Fig. S6–S8). This v range was chosen to account for both short (fast v) and long (slow v) diffusion time scales.

To assess differences in mass-transfer behaviour, the logarithm of the I_{pc} versus the logarithm of v graphs were constructed. Note that if the mass-transfer is semi-infinite in a planar surface, the slope of the plot should be 0.5, while the influence of other diffusion types could result in higher or lower values. For semi-infinite planar diffusion, peak current is proportional to the square root of v, according to the Randles–Ševčík equation:[29,31]

$$\begin{aligned} I_{pc} &= K_{const} v^{\frac{1}{2}} \leftrightarrow \log(I_{pc}) = \log\left(K_{const} v^{\frac{1}{2}}\right) \\ &= \log\left(v^{\frac{1}{2}}\right) + \log(K_{const}) = \frac{1}{2}\log(v) + \log(K_{const}) \end{aligned} \qquad (3)$$

where

$$K_{const} = (2.69 \times 10^5) n^{\frac{3}{2}} A D^{\frac{1}{2}} C \qquad (4)$$

n is the number of electrons, A is the electroactive area in cm^2, and C is the concentration of the electroactive species in mol cm^{-3}. The slope of the $\log(I_{pc})$ vs. $\log(v)$ curve should be equal to 0.5. On the other hand, if thin-layer voltammetry conditions apply, peak current is proportional to v according to:[29]

$$I_{pc} = K_{const}v \leftrightarrow \log(I_{pc}) = \log(K_{const}v) = \log(v) + \log(K_{const}) \tag{5}$$

where

$$K_{const} = \frac{n^2 F^2 VC}{4RT} \tag{6}$$

F is Faraday's constant (96 485 C mol), V is the thin layer volume in cm^3, C is the concentration of the electroactive species in mol cm^{-3}, R is the gas constant (8.314 J mol^{-1} K^{-1}) and T is the temperature (K). The slope of the $\log(I_{pc})$ *vs.* $\log(v)$ curve should be equal to 1. Finally, under the sole influence of radial diffusion, peak current is completely independent of v, as per:[29]

$$I_{pc} = K_{const} \leftrightarrow \log(I_{pc}) = \log(K_{const}) \tag{7}$$

where

$$K_{const} = 4nFrCD \tag{8}$$

r is the radius of the uncovered (active) part of the electrode in cm. Since there is no dependence between the two, the slope of the $\log(I_{pc})$ *vs.* $\log(v)$ curve should be equal to 0. For all the electrodes before biofilm growth, a slope of 0.5 is expected, although surface roughness, hydrophobicity and other surface-related factors could reduce this value marginally.[31]

Fig. 5 shows the $\log(I_{pc})$ *vs.* $\log(v)$ plots for (A) TC-pSi, (B) PC-pSi, and (C) THC-pSi. For TC-pSi before biofilm growth, the slope is 0.52 ± 0.01 which is considered to be under the influence of linear diffusion. After 24 h of biofilm growth, a slope of 0.45 ± 0.01 is exhibited, where linear diffusion is still predominant. Similarly, 0.43 ± 0.01 and 0.45 ± 0.01 values were reached at 48 h and 72 h, respectively. Considering the factors discussed above, it can be concluded that linear diffusion is predominant throughout the biofilm growth process, which in turn dictates the biofilm growth on TC-pSi occurs uniformly, even at the earliest growth stage.

For PC-pSi before biofilm growth, a slope of 0.56 ± 0.01 is shown which can be considered to be under the influence of linear diffusion. However, after 24 h of biofilm growth, a very different behaviour can be seen where the slope decreases to 0.33 ± 0.03 for slow v (5–100 mV s^{-1}), while it rises to 0.72 ± 0.02 for faster v (200–500 mV s^{-1}). Considering the respective confocal image depicted in Fig. 1D, it is hypothesised that the micrometer-sized gaps of exposed PC-pSi surface that emerge during the early biofilm growth, behave as microdisks with radial diffusion being the predominant force of mass-transfer in a long time scale (slow v). However, the slope value of 0.72 ± 0.0 suggests that at high v, there is joint impact of linear diffusion and thin-layer behaviour. This can be attributed to some Ruhex molecules becoming confined in the micrometer-sized gaps while others are still linearly diffused. For the 48 h and 72 h growth stages, slope values are 0.49 ± 0.01 and 0.45 ± 0.01, respectively, along the whole v range (5–500 mV s^{-1}). Considering the factors discussed above, it can be concluded that linear diffusion is predominant for the 48 h and 72 h stages of the biofilm growth process, indicating that the micro-sized gaps emerging at 24 h were completely covered at later stages, forming a uniform biofilm.

For bare THC-pSi, the slope value shown (0.42 ± 0.01) agrees with a system where the sole influence of linear diffusion applies. However, after 24 h of biofilm growth, a very different behaviour can be observed where the slope is *ca.* 0.31 ± 0.03 for slow v (5–100 mV s^{-1}) while it rises to 0.63 ± 0.02 for faster v (200–500 mV s^{-1}). Similar to the results discussed for PC-pSi, based on the observations of the confocal image in Fig. 1H, it is possible to attribute the micrometer-sized gaps of exposed THC-pSi surface that emerge during the early biofilm growth, to THC-pSi behaving as microdisks with radial diffusion being the predominant force of mass-transfer in long time scales (small v). However, the slope value of 0.63 ± 0.02 suggests that at high v, there could be a joint impact of linear diffusion and thin-layer behavior, like the results observed for PC-pSi, likely attributed to the confinement of some Ruhex molecules in the micrometer-sized gaps, and the linear diffusion of others towards the electrode surface. However, at increasing growth stages, it is evident that for slow v (5–100 mV s^{-1}) linear diffusion is marginally more dominant than before for 48 h (0.33 ± 0.03), and largely more dominant at 72 h (0.41 ± 0.01). At faster v (200–500 mV s^{-1}), radial diffusion is more actively present (0.21 ± 0.02) for 48 h, and almost exclusively present (0.07 ± 0.05) for 72 h. This seems to confirm that in these cases
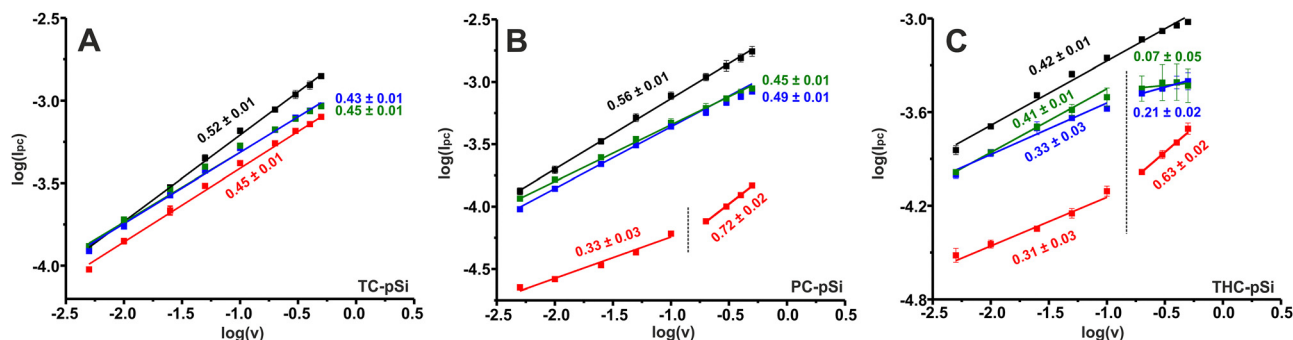

Fig. 5 Log (I_{pc}) *vs.* log(v) plots with the corresponding slopes for (A) TC-pSi, (B) PC-pSi, and (C) THC-pSi. Coloured symbols indicate: black – bare electrode, red – at 24 h biofilm growth, blue – at 48 h biofilm growth, and green – at 72 h biofilm growth. Error bars represent the standard deviation of the measurements for three electrodes.

This journal is © The Royal Society of Chemistry 2025

J. Mater. Chem. B, 2025, **13**, 11284–11297 | **11291**

no confinement of the Ruhex species occurs in the gaps, which are still present even if the biofilm growth has become more uniform than that of the 24 h specimen.

At this point, we can reliably use both $\Theta\%$ and the slopes calculated above to discuss in depth the differences in behaviour observed for each one of the C-pSi platforms assessed.

For TC-pSi, $\Theta\%$ values are relatively small throughout the biofilm growth process, with linear diffusion being always predominant. According to the theory discussed above, this means that biofilms on TC-pSi steadily increase their homogeneity throughout their growth, as underpinned by the constant decrease in $\Theta\%$. Taking into account the respective confocal images displayed in Fig. 1A–C, the emergence of arrays of sub-micrometer-sized blocks is predominant for all time points.

For PC-pSi, $\Theta\%$ values are high at the first 24 h of biofilm growth, with radial diffusion playing a key role at relatively low v (5–100 mV s^{-1}). Conversely, at higher v (200–500 mV s^{-1}) there is a joint effect of linear diffusion and thin-layer reactions. This information can be used to qualitatively assess the morphological characteristics of the biofilm, by considering the diffusion layer thickness (L) as follows.

Knowing that radial diffusion is prevalent between v of 5–100 mV s^{-1}, we can calculate L using eqn (2), leading to values ranging from 358.7 to 86.2 μm. To sustain radial diffusion over this range means that d_0 should be less than 86 μm, while D_0 should be larger than 359 μm. Knowing that at 200 mV s^{-1} (L = 62 μm) radial diffusion ceases to intervene allows us to estimate that d_0 should be between 86 and 62 μm. This information supports biofilm growth at this stage leading to the formation of micro-sized blocks of great thickness, which completely inhibit mass-transfer at the blocked sites and forces radial diffusion at the edges of the remaining active sites.

At later growth stages (48 h and 72 h) the biofilm behaviour closely resembles that of the respective TC-pSi substrate (albeit with greater surface coverage) at the same time points. This means that the biofilm grown on PC-pSi acts as a single macroblock with increasing homogeneity throughout its growth stage, what is supported by the decrease in the $\Theta\%$ observed between 48 h and 72 h of growth.

For THC-pSi, similarly to PC-pSi, $\Theta\%$ values are high at the first 24 h of biofilm growth, with radial diffusion being predominant at relatively low v (5–100 mV s^{-1}). Similar conclusions can be drawn as with the corresponding PC-pSi electrodes (60 < d_0 < 85 μm and D_0 > 393 μm).

For biofilms grown for 48 h on THC-pSi, radial diffusion contributes at relatively low v (5–100 mV s^{-1}), becoming even more predominant at higher v (200–500 mV s^{-1}). This means that smaller microblocks than the ones present at 24 h exist in this case (d_0 < 40 μm), and since radial diffusion is present even for the largest value of L (359 μm), we can assume that D_0 > 359 μm. In simple terms, at 48 h smaller active parts than those shown at 24 h emerge, spaced almost equally apart as before.

Finally, at 72 h the biofilm behaves similarly to the respective TC-pSi, with linear diffusion being predominant at the lower v (5–100 mV s^{-1}), while radial diffusion reigns almost completely at the higher v (200–500 mV s^{-1}). This means that in contrast with the previous time points, homogeneity increases, as supported by the decrease in $\Theta\%$ between 48 h and 72 h, and d_0 < 41 μm and D_0 < 62 μm. This means that in this case the active parts remain small, but are placed closer to each other than before.

To complete the electrochemical analysis of the three types of C-pSi with *S. epidermidis* biofilms grown on their surface, EIS measurements were taken at the same time points of biofilm growth. Equivalent circuit fitting was used for all three electrodes and their respective biofilm growth time points. To avoid complexities, the well-known Randles circuit was taken as a reference point[32] when complex circuits were employed. Randles circuit comprises the uncompensated or solution resistance (R_s), set in series with the double-layer capacitance of the electrode (depending on various morphological parameters can be either a plain capacitor – C, or a constant phase element – CPE), the latter being parallel to the charge-transfer resistance (R_{ct}), set in series to the Warburg impedance (Z_w), which is a defined CPE accounting for semi-infinite diffusion.[33] The equivalent circuit employed for each case is depicted below each Nyquist plot (Fig. 6), together with graphical illustrations of the corresponding biofilm topology. The equivalent circuits used to fit EIS data obtained using bare C-pSi electrodes are shown in Fig. S9. The values of each electrochemical parameter produced through the equivalent circuit fitting are listed in Table S1.

Starting with TC-pSi, it can be seen that similar conclusions to those reached *via* the CV analysis can be drawn. Prior to biofilm growth, TC-pSi behaves almost like a Randles circuit, with the exception that an additional CPE is added to account for the capacitance of the nanoporous carbon film (termed CPE_f – f stands for "film").[34] Next, to fit EIS data obtained at the three growth stages (24 h, 48 h and 72 h), a regular Randles circuit is used which implies that the biofilm growth occurs in a very homogeneous fashion (there is only one electrode/electrolyte interface during growth), and the biofilm is thin enough to allow faradaic reactions (albeit with an increase in R_{ct}, which can be considered to be similar for all three time points). Note that a thicker coating is expected to create two interfaces or inhibit charge-transfer resistance more dramatically.[34] Regarding the respective PC-pSi Nyquist plots, the equivalent circuit analysis before biofilm growth uses a modified-Randles circuit with an additional CPE_f, like in the case of TC-pSi, due to the same reason.[24] Moreover, at the 24 h growth stage, there is a sharp increase of the time constant (shown by the emergence of a vast semi-circle), which can be correlated to the great coverage caused by the biofilm, presumably featuring a very thick coating with pinholes. This behaviour is very different from that shown by TC-pSi at the same growth stage. While the biofilm on TC-pSi is thin enough to allow the transfer of faradaic current uniformly (possibly through tunnelling effects), in the case of PC-pSi the biofilm is thick enough to partially inhibit charge transfer, though there is still charge transfer through the uncovered part of the electrode. This dual behaviour is modelled by the addition of an additional R_f–CPE_f in series circuit, as the "blocking"
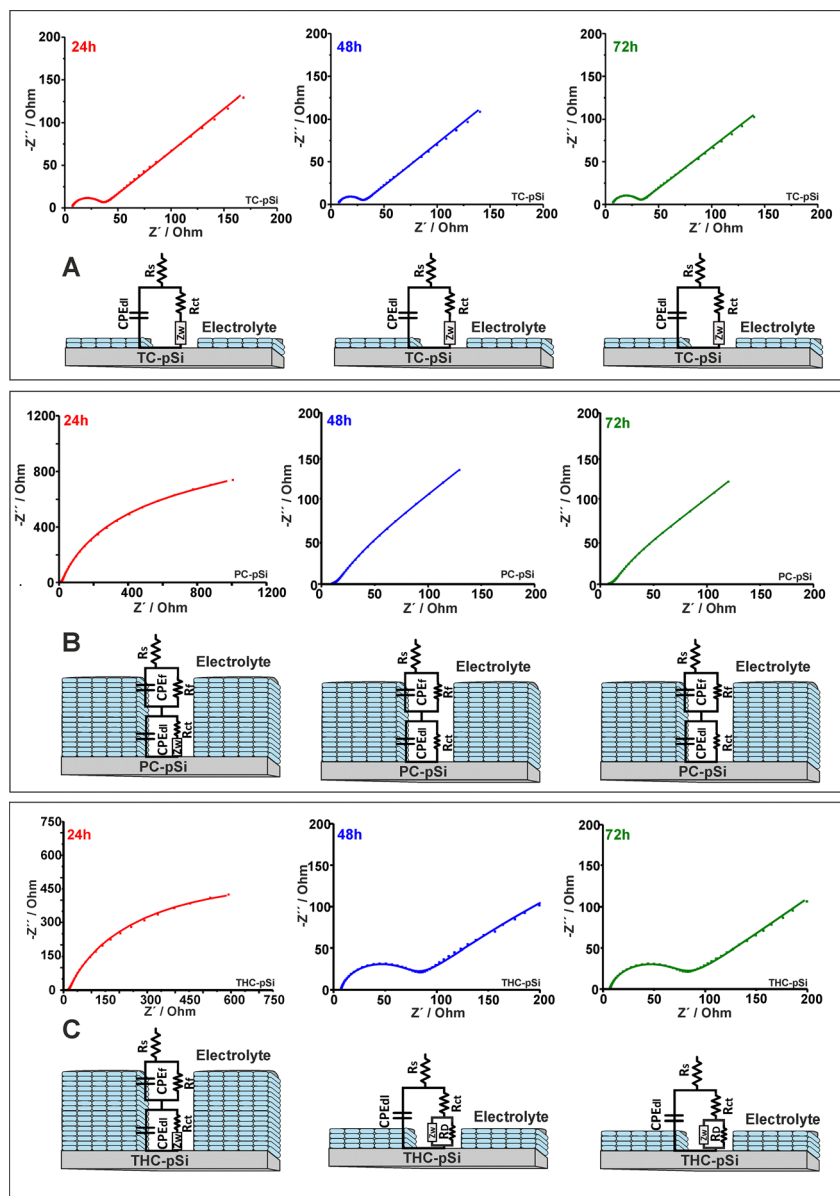
Fig. 6 Nyquist plots obtained using (A) TC–pSi, (B) PC–pSi, and (C) THC–pSi as the working electrode, measured at different stages of biofilm growth, in the presence of 10 mM Ruhex. Graphical illustrations of the biofilm growth state along with the respective equivalent circuits are included under each plot. Electrolyte: 100 mM PBS. DC potential: −0.2 V.

interface, and by the inner Randles circuit to account for the charge transfer through the non-covered part of the electrode. At 48 h and 72 h of biofilm growth, the system is modelled by the same circuit, even though there is a great reduction in R_{ct}, which can be attributed to the reconfiguration of the biofilm over time into a thinner, more homogeneous coating. However, in contrast with TC-pSi, "blocking" areas are still present, admittedly to a smaller degree. Finally, regarding THC-pSi, the bare electrode shows Randles behaviour. Nonetheless, after 24 h of biofilm growth, similar to the behaviour shown by PC-pSi, a large semicircle emerges, attributed to the coverage caused by the thick biofilm. However, at 48 h and 72 h of biofilm growth, THC-pSi stands as a middle ground between TC-pSi and PC-pSi. This is because THC-pSi is modelled using a Randles circuit similar to

that used to model TC-pSi, which accounts for the thin part of the biofilm. However, unlike TC-pSi, mass transfer is not purely linear, which is evident from the deviation of the $<45°$ diffusion impedance (at semi-infinite linear diffusion, the slope of the low frequency part is at 45°),[33] behaviour attributed to hemispherical diffusion and modelled by an additional resistance (R_D) set in parallel to the Warburg impedance. This is a well-known modification of the Warburg impedance[35] according to which, the same treatment as in eqn (2) can be given with $L = \sqrt{\pi D t} = \sqrt{\frac{D}{\pi f}}$, with the lowest frequency f used in the measurement being 0.1 Hz, L equals 53.8 μm. This means that $d_0 < 53.8$ μm, while $D_0 > 53.8$ μm. This is in accordance with the respective CV analysis.

This journal is © The Royal Society of Chemistry 2025

J. Mater. Chem. B, 2025, **13**, 11284–11297 | **11293**

Similarly to PC-pSi, there is still a portion of thick biofilm coating which, however, is disbanded, enabling the penetration of the redox species, and by extension the contribution of radial (or hemispherical) diffusion onto the pinholes. This is in line with the contribution of radial diffusion previously discussed in the CV analysis. Such effect is modelled by the inclusion of an additional diffusion resistance (R_D) in parallel with the Warburg impedance of the rest of the Randles circuit, which stands for the thinner, homogeneous part of the biofilm, similar to TC-pSi. Table 1 entails a summary of all the parameters extracted from the various characterisations presented in this section.

3.4. Technique cross-referencing

There is no consensus yet on the technique to be used as the "gold standard" for biofilm detection and characterisation. By combining the various techniques used in this work, their shortcomings are counterbalanced.

While the majority of the presented techniques have been either solely or in parallel used to characterise bacterial biofilms, electrochemical techniques have never been used in such a fashion before to extract specific morphological information. In this instance, the suitability of the C-pSi platforms to act as biofilm scaffolds and their tunable wettability led to the extraction of profitable information through the exploitation of different diffusion characteristics governing each one. These characteristics were directly correlated to the morphological aspects of the respective biofilm growth patterns. In turn, those patterns were translated to a variety of electrochemical outputs which were identified with CV analysis at increasing v and EIS through equivalent circuit fitting. In the end, it was possible to estimate

Table 1 Summary of all characteristic features for each C-pSi substrate

	Pore diameter (nm)			
Substrate	Before biofilm	24 h	48 h	72 h
TC-pSi	34 ± 7			
PC-pSi	21 ± 5		N/A	
THC-pSi	42 ± 13			

	Pore depth (µm)			
	Before biofilm	24 h	48 h	72 h
TC-pSi	3.5			
PC-pSi	3.5		N/A	
THC-pSi	3.5			

	Contact angle (°)			
	Before biofilm	24 h	48 h	72 h
TC-pSi	30.4 ± 1.3			
PC-pSi	50.7 ± 3.7		N/A	
THC-pSi	95.9 ± 3.3			

	Biofilm thickness (µm)			
	Before biofilm	24 h	48 h	72 h
TC-pSi		24.4 ± 6.5	8.1 ± 1.0	6.1 ± 0.8
PC-pSi	N/A	10.6 ± 0.2	11.4 ± 2.5	8.1 ± 1.4
THC-pSi		8.9 ± 1.0	10.0 ± 1.5	10.2 ± 0.5

	Surface coverage %			
	Before biofilm	24 h	48 h	72 h
TC-pSi		59.3 ± 21.8	97.8 ± 1.1	99.4 ± 0.4
PC-pSi	N/A	86.7 ± 4.2	98.1 ± 0.6	97.5 ± 2.1
THC-pSi		94.5 ± 3.2	94.5 ± 8.5	99.0 ± 0.6

	Slope of $\log I_{pc}$ vs. $\log v$			
	Before biofilm	24 h	48 h	72 h
TC-pSi	0.52 ± 0.01	0.45 ± 0.01	0.43 ± 0.01	0.45 ± 0.01
PC-pSi	0.56 ± 0.01	0.33 ± 0.03 (0.72 ± 0.02)	0.49 ± 0.01	0.45 ± 0.01
THC-pSi	0.42 ± 0.01	0.31 ± 0.03 (0.63 ± 0.02)	0.33 ± 0.03 (0.21 ± 0.02)	0.41 ± 0.01 (0.07 ± 0.05)

	R_{ct}/Ohm			
	Before biofilm	24 h	48 h	72 h
TC-pSi	7.496	27.26	21.81	25.03
PC-pSi	34.96	13.68	3.413	3.287
THC-pSi	14.46	8.961	69.13	71.02

11294 | J. Mater. Chem. B, 2025, **13**, 11284–11297

This journal is © The Royal Society of Chemistry 2025

Table 2 Summary of the biofilm characterisation techniques used in this work and the corresponding information obtained

Parameter	Technique				Comments
	ESEM	CLSM	CV	EIS	
Morphological analysis	✓	✓			Bacteria existence, shape, and growth patterns
3D analysis		✓			x, y and z planes are imaged, rendering 3D models
Cell viability		✓			Discrimination and spatial distribution of alive and dead bacteria
Biofilm thickness		✓			Mean biofilm thickness calculated from confocal z-stacks
Surface coverage		✓	✓		Biofilm surface coverage calculated using (i) ImageJ by eliminating the background, and (ii) the electrochemical response before and after coverage
Impact of morphology on diffusion			✓	✓	Influence of different morphological growth patterns (*e.g.*, mushroom-like growth, patchy growth, *etc.*) on the diffusion of electroactive species, enabling the estimation of the relative dimensions of individual areas

the relative dimensions of individual areas and correlate them with the CLSM images. This task is not attainable with simple electron microscopy techniques such as ESEM. CLSM can provide similar information, but obviously requires extensive sample preparation and data analysis. Table 2 highlights the specific information provided by each one of those techniques, confirming the abundancy of information that can be extracted using electrochemical techniques for biofilms grown on C-pSi.

4. Conclusions

We have successfully demonstrated the potential of three types of C-pSi substrates to act with a dual function, as bacterial biofilm scaffolds and electrochemical transducers to sense biofilm growth. Hydrophobic THC-pSi, hydrophilic TC-pSi and mildly hydrophilic PC-pSi have been proven to exhibit vastly different characteristics towards bacterial biofilm formation and their associated electrochemical response.

The presence of biofilm on the C-pSi surface was confirmed by ESEM and CLSM. Combining LIVE/DEAD™ staining with CLSM the biofilm growth patterns and various morphological features were also visualised. Regarding the electrochemical analysis, CV measurements in the presence of a redox probe showed changes in intensity current in the presence of biofilm grown on the electrode surface. An expected trend of an initial decrease in peak current was followed by an unexpected increase in the current intensities for all substrates. Further investigation into this phenomenon by analysing the measured current in a range of scan rates revealed that the presence of biofilm and its formation process influence the mass transfer behavior. Moreover, determining the type of diffusion that is dominant can be used as a proxy for the growth pattern of the biofilm. EIS analysis corroborated these findings by denoting whether a single interface between the electrode/electrolyte or a dual interface between some active areas and the electrolyte, and other inactive (biofilm covered) areas and the electrolyte is present. Where biofilm growth was observed to be homogenous, linear diffusion was dominant and where the growth was "patchy" with micrometer-sized gaps, radial diffusion was observed.

Table S2 summarises the information obtained from each technique used in this work when evaluating each one of the C-pSi tested.

To move beyond the technical aspects of the analysis, the important achievements of this work are summarised below.

The ability of the C-pSi to act as biofilm scaffolds was proved and was unrelated to their differences in wettability. However, these differences play a big role in the initial attachment of bacteria, the morphology of the biofilm, and the dead/alive bacteria analogy.

It was proven that the most hydrophilic C-pSi (TC-pSi) is more hospitable to bacteria considering the large number of alive bacteria on it after 24 h, the homogeneity of the biofilm even at the first stage of growth, which was proved both using CLSM and a variety of electrochemical techniques. From a sensing standpoint, the hospitability of TC-pSi for the bacterial biofilm, enables its detection, but prevents the discrimination between different growth stages.

When more hydrophobic platforms were employed, diverse morphological and electrochemical patterns were created which were accurately correlated and used to effectively discriminate between each growth stage. The immense difference between the initial growth stage (24 h) and the later stages paves the way to using these hydrophobic (or more accurately, less hydrophilic) C-pSi substrates to create a tool which can singlehandedly discriminate these patterns accurately and quickly.

As a last remark, while there is no doubt that CLSM provides a very concrete image of the growth patterns and behaviour, it requires costly, difficult-to-find and operate instrumentation. Our findings conclusively prove that these patterns can be effectively distinguished through electrochemical analysis. Moreover, this kind of analysis can be performed with common, simple and cost-effective instrumentation, exhibiting high performance when combined with advanced nanostructured platforms such as the C-pSi. Considering the portability of modern-day electrochemical apparatus, this work is a solid steppingstone for the use of the method here reported in the point-of-need.

Author contributions

Fearghal O'Connor: investigation, data curation, methodology, and writing – original draft. Alexandros Lazanas: investigation, data curation, methodology, supervision, and writing – reviewing and editing. Beatriz Prieto Simón: conceptualization, methodology,

supervision, funding acquisition, and writing – reviewing and editing.

Conflicts of interest

There are no conflicts to declare.

Data availability

The data that support the findings of this study are available from the corresponding author, B. P. S., upon reasonable request.

Supplementary information: Additional experimental details and results including: protocols for *S. epidermidis* stocks preparation and biofilm growth on C-pSi, FESEM images and water contact angle photographs of all types of C-pSi, ESEM images of each C-pSi at different time points of biofilm growth, CLSM images of C-pSi control groups, plots of the mean values of the thickness of biofilms grown on each C-pSi, CV responses at increasing scan rates obtained for each C-pSi at different time points of biofilm growth, Nyquist plots obtained for each C-pSi and the equivalent circuit fitting parameters calculated from them, and a summary of the conclusions obtained using each characterisation technique for each C-pSi platform tested. See DOI: https://doi.org/10. 1039/d5tb01036e.

Acknowledgements

References

1 D. Lopez, H. Vlamakis and R. Kolter, *Cold Spring Harbor Perspect. Biol.*, 2010, **2**, a000398.

2 M. E. Davey and G. A. O'toole, *Microbiol. Mol. Biol. Rev.*, 2000, **64**, 847–867.

3 J. W. Costerton, Z. Lewandowski, D. E. Caldwell, D. R. Korber and H. M. Lappin-Scott, *Annu. Rev. Microbiol.*, 1995, **49**, 711–745.

4 H.-C. Flemming and J. Wingender, *Nat. Rev. Microbiol.*, 2010, **8**, 623–633.

5 K. Sauer, P. Stoodley, D. M. Goeres, L. Hall-Stoodley, M. Burmølle, P. S. Stewart and T. Bjarnsholt, *Nat. Rev. Microbiol.*, 2022, **20**, 608–620.

6 S. Afrasiabi and A. Partoazar, *Front. Microbiol.*, 2024, **15**, 1387114.

7 S. Sharma, J. Mohler, S. D. Mahajan, S. A. Schwartz, L. Bruggemann and R. Aalinkeel, *Microorganisms*, 2023, **11**, 1614.

8 C. Michaelis and E. Grohmann, *Antibiotics*, 2023, **12**, 328.

9 H. Y. Liu, E. L. Prentice and M. A. Webber, *Npj Antimicrob. Resist.*, 2024, **2**, 27.

10 H.-C. Flemming, J. Wingender, U. Szewzyk, P. Steinberg, S. A. Rice and S. Kjelleberg, *Nat. Rev. Microbiol.*, 2016, **14**, 563–575.

11 H.-C. Flemming, J. Wingender, U. Szewzyk, P. Steinberg, S. A. Rice and S. Kjelleberg, *Nat. Rev. Microbiol.*, 2016, **14**, 563–575.

12 M. Cámara, W. Green, C. E. MacPhee, P. D. Rakowska, R. Raval, M. C. Richardson, J. Slater-Jefferies, K. Steventon and J. S. Webb, *NPJ Biofilms Microbiomes*, 2022, **8**, 42.

13 Y. T. H. Dang, A. Power, D. Cozzolino, K. B. Dinh, B. S. Ha, A. Kolobaric, J. Vongsvivut, V. K. Truong and J. Chapman, *J. Bio- Tribo-Corros.*, 2022, **8**, 50.

14 M. K. Pal and M. Lavanya, *J. Bio-Tribo-Corros.*, 2022, **8**, 76.

15 R. D. Wolcott, K. P. Rumbaugh, G. James, G. Schultz, P. Phillips, Q. Yang, C. Watters, P. S. Stewart and S. E. Dowd, *J. Wound Care*, 2010, **19**, 320–328.

16 Z. Khatoon, C. D. McTiernan, E. J. Suuronen, T.-F. Mah and E. I. Alarcon, *Heliyon*, 2018, **4**, e01067.

17 G. Sharma, S. Sharma, P. Sharma, D. Chandola, S. Dang, S. Gupta and R. Gabrani, *J. Appl. Microbiol.*, 2016, **121**, 309–319.

18 S. Rana and L. S. B. Upadhyay, *Indian J. Microbiol.*, 2023, **63**, 299–306.

19 J. Azeredo, N. F. Azevedo, R. Briandet, N. Cerca, T. Coenye, A. R. Costa, M. Desvaux, G. Di Bonaventura, M. Hébraud, Z. Jaglic, M. Kačániová, S. Knøchel, A. Lourenço, F. Mergulhão, R. L. Meyer, G. Nychas, M. Simões, O. Tresse and C. Sternberg, *Crit. Rev. Microbiol.*, 2017, **43**, 313–351.

20 L. Liu, Y. Xu, F. Cui, Y. Xia, L. Chen, X. Mou and J. Lv, *Biosens. Bioelectron.*, 2018, **112**, 86–92.

21 F.-G. Bănică, Chemical Sensors Based on Microorganisms, Living Cells and Tissues, in *Chemical Sensors and Biosensors*, ed. F.-G. Bănică, 2012, pp. 518–529.

22 M. Sabaté Brescó, L. G. Harris, K. Thompson, B. Stanic, M. Morgenstern, L. O'Mahony, R. G. Richards and T. F. Moriarty, *Front. Microbiol.*, 2017, **8**, 1401.

23 K. Guo, A. Sharma, R. J. Toh, E. Alvárez de Eulate, T. R. Gengenbach, X. Cetó, N. H. Voelcker and B. Prieto- Simón, *Adv. Funct. Mater.*, 2019, **29**, 1809206.

24 A. A. Rajendran, K. Guo, A. Alvarez-Fernandez, T. R. Gengenbach, M. B. Velasco, M. J. Fornerod, K. Shafique, M. Füredi, P. Formentín, H. Haji-Hashemi, S. Guldin, N. H. Voelcker, X. Cetó and B. Prieto-Simón, *Mater. Today Adv.*, 2024, **21**, 100464.

25 R. L. McCreery, *Chem. Rev.*, 2008, **108**, 2646–2687.

11296 | *J. Mater. Chem. B*, 2025, **13**, 11284–11297

This journal is © The Royal Society of Chemistry 2025

26 J. Salonen, M. Björkqvist, E. Laine and L. Niinistö, *Appl. Surf. Sci.*, 2004, **225**, 389–394.

27 G. Steinbach, C. Crisan, S. L. Ng, B. K. Hammer and P. J. Yunker, *J. R. Soc., Interface*, 2020, **17**, 20200486.

28 Z. Wang, X. Gong, J. Xie, Z. Xu, G. Liu and G. Zhang, *Langmuir*, 2019, **35**, 7405–7413.

29 A. J. Bard, L. R. Faulkner and H. S. White, *Electrochemical methods: Fundamentals and Applications*, John Wiley & Sons, Ltd, 3rd edn, 2022.

30 In Understanding Voltammetry, World ScientifiC (Europe), 2017, pp. 203–244.

31 M. G. Trachioti, A. Ch Lazanas and M. I. Prodromidis, *Microchim. Acta*, 2023, **190**, 251.

32 J. E. B. Randles, *Discuss. Faraday Soc.*, 1947, **1**, 11–19.

33 A. C. Lazanas and M. I. Prodromidis, *ACS Meas. Sci. Au*, 2023, **3**, 162–193.

34 M. E. Orazem and B. Tribollet, Equivalent Circuit Analogs, in *Electrochemical Impedance Spectroscopy*, ed. M. E. Orazem and B. Tribollet, 2017, pp. 191–206.

35 F. Scholtz, *Electroanalytical Methods, Guide to Experiments and Applications 2nd, revised and extended edition*, Springer, Verlag Berlin Heidelberg, 2010.